Measurement of angular asymmetries in the decays $B \to K^* \ell^+ \ell^-$

J. P. Lees,[1] V. Poireau,[1] V. Tisserand,[1] E. Grauges,[2] A. Palano,[3a,3b] G. Eigen,[4] B. Stugu,[4] D. N. Brown,[5] L. T. Kerth,[5] Yu. G. Kolomensky,[5] M. J. Lee,[5] G. Lynch,[5] H. Koch,[6] T. Schroeder,[6] C. Hearty,[7] T. S. Mattison,[7] J. A. McKenna,[7] R. Y. So,[7] A. Khan,[8] V. E. Blinov,[9a,9b,9c] A. R. Buzykaev,[9a] V. P. Druzhinin,[9a,9b] V. B. Golubev,[9a,9b] E. A. Kravchenko,[9a,9b] A. P. Onuchin,[9a,9b,9c] S. I. Serednyakov,[9a,9b] Yu. I. Skovpen,[9a,9b] E. P. Solodov,[9a,9b] K. Yu. Todyshev,[9a,9b] A. J. Lankford,[10] B. Dey,[11] J. W. Gary,[11] O. Long,[11] M. Franco Sevilla,[12] T. M. Hong,[12] D. Kovalskyi,[12] J. D. Richman,[12] C. A. West,[12] A. M. Eisner,[13] W. S. Lockman,[13] W. Panduro Vazquez,[13] B. A. Schumm,[13] A. Seiden,[13] D. S. Chao,[14] C. H. Cheng,[14] B. Echenard,[14] K. T. Flood,[14] D. G. Hitlin,[14] T. S. Miyashita,[14] P. Ongmongkolkul,[14] F. C. Porter,[14] M. Röhrken,[14] R. Andreassen,[15] Z. Huard,[15] B. T. Meadows,[15] B. G. Pushpawela,[15] M. D. Sokoloff,[15] L. Sun,[15] P. C. Bloom,[16] W. T. Ford,[16] A. Gaz,[16] J. G. Smith,[16] S. R. Wagner,[16] R. Ayad,[17,†] W. H. Toki,[17] B. Spaan,[18] D. Bernard,[19] M. Verderi,[19] S. Playfer,[20] D. Bettoni,[21a] C. Bozzi,[21a] R. Calabrese,[21a,21b] G. Cibinetto,[21a,21b] E. Fioravanti,[21a,21b] I. Garzia,[21a,21b] E. Luppi,[21a,21b] L. Piemontese,[21a] V. Santoro,[21a] A. Calcaterra,[22] R. de Sangro,[22] G. Finocchiaro,[22] S. Martellotti,[22] P. Patteri,[22] I. M. Peruzzi,[22] M. Piccolo,[22] A. Zallo,[22] R. Contri,[23a,23b] M. R. Monge,[23a,23b] S. Passaggio,[23a] C. Patrignani,[23a,23b] B. Bhuyan,[24] V. Prasad,[24] A. Adametz,[25] U. Uwer,[25] H. M. Lacker,[26] U. Mallik,[27] C. Chen,[28] J. Cochran,[28] S. Prell,[28] H. Ahmed,[29] A. V. Gritsan,[30] N. Arnaud,[31] M. Davier,[31] D. Derkach,[31] G. Grosdidier,[31] F. Le Diberder,[31] A. M. Lutz,[31] B. Malaescu,[31,‡] P. Roudeau,[31] A. Stocchi,[31] G. Wormser,[31] D. J. Lange,[32] D. M. Wright,[32] J. P. Coleman,[33] J. R. Fry,[33] E. Gabathuler,[33] D. E. Hutchcroft,[33] D. J. Payne,[33] C. Touramanis,[33] A. J. Bevan,[34] F. Di Lodovico,[34] R. Sacco,[34] G. Cowan,[35] D. N. Brown,[36] C. L. Davis,[36] A. G. Denig,[37] M. Fritsch,[37] W. Gradl,[37] K. Griessinger,[37] A. Hafner,[37] K. R. Schubert,[37] R. J. Barlow,[38,§] G. D. Lafferty,[38] R. Cenci,[39] B. Hamilton,[39] A. Jawahery,[39] D. A. Roberts,[39] R. Cowan,[40] R. Cheaib,[41] P. M. Patel,[41,*] S. H. Robertson,[41] N. Neri,[42a] F. Palombo,[42a,42b] L. Cremaldi,[43] R. Godang,[43,‖] D. J. Summers,[43] M. Simard,[44] P. Taras,[44] G. De Nardo,[45a,45b] G. Onorato,[45a,45b] C. Sciacca,[45a,45b] G. Raven,[46] C. P. Jessop,[47] J. M. LoSecco,[47] K. Honscheid,[48] R. Kass,[48] M. Margoni,[49a,49b] M. Morandin,[49a] M. Posocco,[49a] M. Rotondo,[49a] G. Simi,[49a,49b] F. Simonetto,[49a,49b] R. Stroili,[49a,49b] S. Akar,[50] E. Ben-Haim,[50] M. Bomben,[50] G. R. Bonneaud,[50] H. Briand,[50] G. Calderini,[50] J. Chauveau,[50] Ph. Leruste,[50] G. Marchiori,[50] J. Ocariz,[50] M. Biasini,[51a,51b] E. Manoni,[51a] A. Rossi,[51a] C. Angelini,[52a,52b] G. Batignani,[52a,52b] S. Bettarini,[52a,52b] M. Carpinelli,[52a,52b,¶] G. Casarosa,[52a,52b] M. Chrzaszcz,[52a] F. Forti,[52a,52b] M. A. Giorgi,[52a,52b] A. Lusiani,[52a,52c] B. Oberhof,[52a,52b] E. Paoloni,[52a,52b] M. Rama,[52a] G. Rizzo,[52a,52b] J. J. Walsh,[52a] D. Lopes Pegna,[53] J. Olsen,[53] A. J. S. Smith,[53] F. Anulli,[54a] R. Faccini,[54a,54b] F. Ferrarotto,[54a] F. Ferroni,[54a,54b] M. Gaspero,[54a,54b] A. Pilloni,[54a,54b] G. Piredda,[54a] C. Bünger,[55] S. Dittrich,[55] O. Grünberg,[55] M. Hess,[55] T. Leddig,[55] C. Voß,[55] R. Waldi,[55] T. Adye,[56] E. O. Olaiya,[56] F. F. Wilson,[56] S. Emery,[57] G. Vasseur,[57] D. Aston,[58] D. J. Bard,[58] C. Cartaro,[58] M. R. Convery,[58] J. Dorfan,[58] G. P. Dubois-Felsmann,[58] W. Dunwoodie,[58] M. Ebert,[58] R. C. Field,[58] B. G. Fulsom,[58] M. T. Graham,[58] C. Hast,[58] W. R. Innes,[58] P. Kim,[58] D. W. G. S. Leith,[58] S. Luitz,[58] V. Luth,[58] D. B. MacFarlane,[58] D. R. Muller,[58] H. Neal,[58] T. Pulliam,[58] B. N. Ratcliff,[58] A. Roodman,[58] R. H. Schindler,[58] A. Snyder,[58] D. Su,[58] M. K. Sullivan,[58] J. Va'vra,[58] W. J. Wisniewski,[58] H. W. Wulsin,[58] M. V. Purohit,[59] J. R. Wilson,[59] A. Randle-Conde,[60] S. J. Sekula,[60] M. Bellis,[61] P. R. Burchat,[61] E. M. T. Puccio,[61] M. S. Alam,[62] J. A. Ernst,[62] R. Gorodeisky,[63] N. Guttman,[63] D. R. Peimer,[63] A. Soffer,[63] S. M. Spanier,[64] J. L. Ritchie,[65] R. F. Schwitters,[65] J. M. Izen,[66] X. C. Lou,[66] F. Bianchi,[67a,67b] F. De Mori,[67a,67b] A. Filippi,[67a] D. Gamba,[67a,67b] L. Lanceri,[68a,68b] L. Vitale,[68a,68b] F. Martinez-Vidal,[69] A. Oyanguren,[69] J. Albert,[70] Sw. Banerjee,[70] A. Beaulieu,[70] F. U. Bernlochner,[70] H. H. F. Choi,[70] G. J. King,[70] R. Kowalewski,[70] M. J. Lewczuk,[70] T. Lueck,[70] I. M. Nugent,[70] J. M. Roney,[70] R. J. Sobie,[70] N. Tasneem,[70] T. J. Gershon,[71] P. F. Harrison,[71] T. E. Latham,[71] H. R. Band,[72] S. Dasu,[72] Y. Pan,[72] R. Prepost,[72] and S. L. Wu[72]

(The *BABAR* Collaboration)

[1]*Laboratoire d'Annecy-le-Vieux de Physique des Particules (LAPP), Université de Savoie, CNRS/IN2P3, F-74941 Annecy-Le-Vieux, France*
[2]*Universitat de Barcelona, Facultat de Fisica, Departament ECM, E-08028 Barcelona, Spain*
[3a]*INFN Sezione di Bari, I-70126 Bari, Italy*
[3b]*Dipartimento di Fisica, Università di Bari, I-70126 Bari, Italy*
[4]*University of Bergen, Institute of Physics, N-5007 Bergen, Norway*
[5]*Lawrence Berkeley National Laboratory and University of California, Berkeley, California 94720, USA*
[6]*Ruhr Universität Bochum, Institut für Experimentalphysik 1, D-44780 Bochum, Germany*
[7]*University of British Columbia, Vancouver, British Columbia, Canada V6T 1Z1*
[8]*Brunel University, Uxbridge, Middlesex UB8 3PH, United Kingdom*
[9a]*Budker Institute of Nuclear Physics SB RAS, Novosibirsk 630090, Russia*
[9b]*Novosibirsk State University, Novosibirsk 630090, Russia*
[9c]*Novosibirsk State Technical University, Novosibirsk 630092, Russia*
[10]*University of California at Irvine, Irvine, California 92697, USA*

[11]*University of California at Riverside, Riverside, California 92521, USA*
[12]*University of California at Santa Barbara, Santa Barbara, California 93106, USA*
[13]*University of California at Santa Cruz, Institute for Particle Physics, Santa Cruz, California 95064, USA*
[14]*California Institute of Technology, Pasadena, California 91125, USA*
[15]*University of Cincinnati, Cincinnati, Ohio 45221, USA*
[16]*University of Colorado, Boulder, Colorado 80309, USA*
[17]*Colorado State University, Fort Collins, Colorado 80523, USA*
[18]*Technische Universität Dortmund, Fakultät Physik, D-44221 Dortmund, Germany*
[19]*Laboratoire Leprince-Ringuet, Ecole Polytechnique, CNRS/IN2P3, F-91128 Palaiseau, France*
[20]*University of Edinburgh, Edinburgh EH9 3JZ, United Kingdom*
[21a]*INFN Sezione di Ferrara, I-44122 Ferrara, Italy*
[21b]*Dipartimento di Fisica e Scienze della Terra, Università di Ferrara, I-44122 Ferrara, Italy*
[22]*INFN Laboratori Nazionali di Frascati, I-00044 Frascati, Italy*
[23a]*INFN Sezione di Genova, I-16146 Genova, Italy*
[23b]*Dipartimento di Fisica, Università di Genova, I-16146 Genova, Italy*
[24]*Indian Institute of Technology Guwahati, Guwahati, Assam 781 039, India*
[25]*Universität Heidelberg, Physikalisches Institut, D-69120 Heidelberg, Germany*
[26]*Humboldt-Universität zu Berlin, Institut für Physik, D-12489 Berlin, Germany*
[27]*University of Iowa, Iowa City, Iowa 52242, USA*
[28]*Iowa State University, Ames, Iowa 50011-3160, USA*
[29]*Physics Department, Jazan University, Jazan 22822, Kingdom of Saudi Arabia*
[30]*Johns Hopkins University, Baltimore, Maryland 21218, USA*
[31]*Laboratoire de l'Accélérateur Linéaire, IN2P3/CNRS et Université Paris-Sud 11, Centre Scientifique d'Orsay, F-91898 Orsay Cedex, France*
[32]*Lawrence Livermore National Laboratory, Livermore, California 94550, USA*
[33]*University of Liverpool, Liverpool L69 7ZE, United Kingdom*
[34]*Queen Mary, University of London, London E1 4NS, United Kingdom*
[35]*University of London, Royal Holloway and Bedford New College, Egham, Surrey TW20 0EX, United Kingdom*
[36]*University of Louisville, Louisville, Kentucky 40292, USA*
[37]*Johannes Gutenberg-Universität Mainz, Institut für Kernphysik, D-55099 Mainz, Germany*
[38]*University of Manchester, Manchester M13 9PL, United Kingdom*
[39]*University of Maryland, College Park, Maryland 20742, USA*
[40]*Massachusetts Institute of Technology, Laboratory for Nuclear Science, Cambridge, Massachusetts 02139, USA*
[41]*McGill University, Montréal, Québec, Canada H3A 2T8*
[42a]*INFN Sezione di Milano, I-20133 Milano, Italy*
[42b]*Dipartimento di Fisica, Università di Milano, I-20133 Milano, Italy*
[43]*University of Mississippi, University, Mississippi 38677, USA*
[44]*Université de Montréal, Physique des Particules, Montréal, Québec, Canada H3C 3J7*
[45a]*INFN Sezione di Napoli, I-80126 Napoli, Italy*
[45b]*Dipartimento di Scienze Fisiche, Università di Napoli Federico II, I-80126 Napoli, Italy*
[46]*NIKHEF, National Institute for Nuclear Physics and High Energy Physics, NL-1009 DB Amsterdam, The Netherlands*
[47]*University of Notre Dame, Notre Dame, Indiana 46556, USA*
[48]*Ohio State University, Columbus, Ohio 43210, USA*
[49a]*INFN Sezione di Padova, I-35131 Padova, Italy*
[49b]*Dipartimento di Fisica, Università di Padova, I-35131 Padova, Italy*
[50]*Laboratoire de Physique Nucléaire et de Hautes Energies, IN2P3/CNRS, Université Pierre et Marie Curie-Paris6, Université Denis Diderot-Paris7, F-75252 Paris, France*
[51a]*INFN Sezione di Perugia, I-06123 Perugia, Italy*
[51b]*Dipartimento di Fisica, Università di Perugia, I-06123 Perugia, Italy*
[52a]*INFN Sezione di Pisa, I-56127 Pisa, Italy*
[52b]*Dipartimento di Fisica, Università di Pisa, I-56127 Pisa, Italy*
[52c]*Scuola Normale Superiore di Pisa, I-56127 Pisa, Italy*
[53]*Princeton University, Princeton, New Jersey 08544, USA*
[54a]*INFN Sezione di Roma, I-00185 Roma, Italy*
[54b]*Dipartimento di Fisica, Università di Roma La Sapienza, I-00185 Roma, Italy*
[55]*Universität Rostock, D-18051 Rostock, Germany*
[56]*Rutherford Appleton Laboratory, Chilton, Didcot, Oxon, OX11 0QX, United Kingdom*

[57]CEA, Irfu, SPP, Centre de Saclay, F-91191 Gif-sur-Yvette, France
[58]SLAC National Accelerator Laboratory, Stanford, California 94309 USA
[59]University of South Carolina, Columbia, South Carolina 29208, USA
[60]Southern Methodist University, Dallas, Texas 75275, USA
[61]Stanford University, Stanford, California 94305-4060, USA
[62]State University of New York, Albany, New York 12222, USA
[63]Tel Aviv University, School of Physics and Astronomy, Tel Aviv 69978, Israel
[64]University of Tennessee, Knoxville, Tennessee 37996, USA
[65]University of Texas at Austin, Austin, Texas 78712, USA
[66]University of Texas at Dallas, Richardson, Texas 75083, USA
[67a]INFN Sezione di Torino, I-10125 Torino, Italy
[67b]Dipartimento di Fisica, Università di Torino, I-10125 Torino, Italy
[68a]INFN Sezione di Trieste, I-34127 Trieste, Italy
[68b]Dipartimento di Fisica, Università di Trieste, I-34127 Trieste, Italy
[69]IFIC, Universitat de Valencia-CSIC, E-46071 Valencia, Spain
[70]University of Victoria, Victoria, British Columbia, Canada V8W 3P6
[71]Department of Physics, University of Warwick, Coventry CV4 7AL, United Kingdom
[72]University of Wisconsin, Madison, Wisconsin 53706, USA
(Received 1 September 2015; published 28 March 2016)

We study the lepton forward-backward asymmetry $\mathcal{A}_{FB}$ and the longitudinal K^* polarization F_L, as well as an observable P_2 derived from them, in the rare decays $B \to K^* \ell^+ \ell^-$, where $\ell^+ \ell^-$ is either $e^+ e^-$ or $\mu^+ \mu^-$, using the full sample of 471 million $B\bar{B}$ events collected at the $\Upsilon(4S)$ resonance with the *BABAR*, detector at the PEP-II $e^+ e^-$ collider. We separately fit and report results for the $K^{*0}(892)\ell^+ \ell^-$ and $K^{*+}(892)\ell^+ \ell^-$ final states, as well as their combination $K^* \ell^+ \ell^-$, in five disjoint dilepton mass-squared bins. An angular analysis of $B^+ \to K^{*+} \ell^+ \ell^-$ decays is presented here for the first time.

DOI: 10.1103/PhysRevD.93.052015

I. INTRODUCTION

The decays $B \to K^*(892)\ell^+ \ell^-$, where $K^* \to K\pi$ (hereinafter, unless explicitly stated otherwise, K^* refers generically to the $K^*(892)$) and $\ell^+ \ell^-$ is either an $e^+ e^-$ or $\mu^+ \mu^-$ pair, arise from flavor-changing neutral-current (FCNC) processes, which are forbidden at tree level in the Standard Model (SM). The lowest-order SM processes contributing to these decays are the photon penguin, the Z penguin and the $W^+ W^-$ box diagrams shown in Fig. 1. Their amplitudes are expressed in terms of hadronic form factors and perturbatively calculable effective Wilson coefficients, $C_7^{\rm eff}$, $C_9^{\rm eff}$ and $C_{10}^{\rm eff}$, which represent the electromagnetic penguin diagram, and the vector part and the axial-vector part of the linear combination of the Z penguin and $W^+ W^-$ box diagrams, respectively [1–7]. Non-SM physics may add new penguin and/or box diagrams, as well as possible contributions from new scalar, pseudoscalar, and/or tensor currents, which can contribute at the same order as the SM diagrams, modifying the effective Wilson coefficients from their SM expectations [8–17]. An example of a non-SM physics loop process is shown in Fig. 2; other possible processes could involve e.g., non-SM Higgs, charginos, gauginos, neutralinos and/or squarks. As a function of dilepton mass-squared $q^2 = m^2_{\ell^+ \ell^-}$, the angular distributions in $B \to K^* \ell^+ \ell^-$ decays are notably sensitive to many possible sources of new physics, with several collaborations presenting results over the past few years [18–25].

At any particular q^2 value, the kinematic distribution of the decay products of $B \to K^* \ell^+ \ell^-$ and the CP-conjugate $\bar{B} \to \bar{K}^* \ell^+ \ell^-$ process depends on six transversity amplitudes which, neglecting CP-violating effects and terms of order m_ℓ^2 and higher, can be expressed as a triply differential cross section in three angles: θ_K, the angle between the K and the B directions in the K^* rest frame; θ_ℓ, the angle between the $\ell^+(\ell^-)$ and the $B(\bar{B})$ direction in the $\ell^+ \ell^-$ rest frame; and ϕ, the angle between the $\ell^+ \ell^-$ and

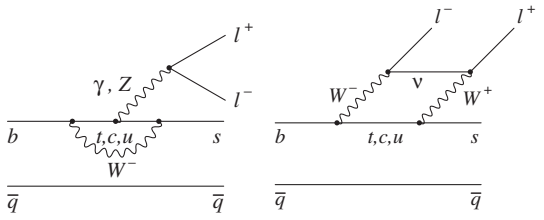

FIG. 1. Lowest-order SM Feynman diagrams for $b \to s\ell^+ \ell^-$.

*Deceased.
†Now at University of Tabuk, Tabuk 71491, Saudi Arabia.
‡Now at Laboratoire de Physique Nucléaire et de Hautes Energies, IN2P3/CNRS, F-75252 Paris, France.
§Now at University of Huddersfield, Huddersfield HD1 3DH, United Kingdom.
‖Now at University of South Alabama, Mobile, Alabama 36688, USA.
¶Also at Università di Sassari, I-07100 Sassari, Italy.

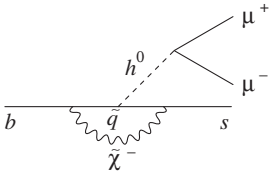

FIG. 2. Feynman diagram of a non-SM Higgs penguin process.

$K\pi$ decay planes in the B rest frame. From the distribution of the angle θ_K obtained after integrating over ϕ and θ_ℓ, we determine the K^* longitudinal polarization fraction F_L using a fit to $\cos\theta_K$ of the form [6]

$$\frac{1}{\Gamma(q^2)}\frac{d\Gamma}{d(\cos\theta_K)} = \frac{3}{2}F_L(q^2)\cos^2\theta_K + \frac{3}{4}(1-F_L(q^2))(1-\cos^2\theta_K). \quad (1)$$

We similarly determine the lepton forward-backward asymmetry $\mathcal{A}_{FB}$ from the distribution of the angle θ_ℓ obtained after integrating over ϕ and θ_K, [6]

$$\frac{1}{\Gamma(q^2)}\frac{d\Gamma}{d(\cos\theta_\ell)} = \frac{3}{4}F_L(q^2)(1-\cos^2\theta_l) + \frac{3}{8}(1-F_L(q^2))(1+\cos^2\theta_l) + \mathcal{A}_{FB}(q^2)\cos\theta_l. \quad (2)$$

We ignore here possible contributions from nonresonant S-wave $B \to K\pi\ell^+\ell^-$ events. The rate for such events has been shown to be consistent with zero [26], with an upper limit (68% C.L.) across the entire dilepton mass-squared range of $< 4\%$ of the $B \to K^*(K\pi)\ell^+\ell^-$ branching fraction [21]. The presence of an S-wave component at this level was shown to lead to a relatively small absolute bias on the order of 0.01 for F_L and $\mathcal{A}_{FB}$; this small bias is ignored here given the relatively larger magnitude of our statistical and systematic uncertainties. Essentially no contributions from low-mass tails of the higher K^* resonances are expected in the $K^*(892)$ mass region considered here.

We ignore small q^2-dependent theory corrections in the large-recoil $q^2 \lesssim 2\ \mathrm{GeV}^2/c^4$ region given the current experimental uncertainties on the angular observables, which are relatively large compared to these small corrections in the underlying SM theory expectations [2]. We determine F_L and $\mathcal{A}_{FB}$ in the five disjoint bins of q^2 defined in Table I. We also present results in a q^2 range $1.0 < q_0^2 < 6.0\ \mathrm{GeV}^2/c^4$, the perturbative window away from the $q^2 \to 0$ photon pole and the $c\bar{c}$ resonances at higher q^2, where theory uncertainties are considered to be under good control. An angular analysis of the decays $B^+ \to K^{*+}\ell^+\ell^-$ is presented here for the first time. We additionally present results for an observable derived from F_L and $\mathcal{A}_{FB}$, $P_2 = (-2/3) * \mathcal{A}_{FB}/(1-F_L)$, with less theory uncertainty, and hence greater sensitivity to non-SM contributions, than either F_L or $\mathcal{A}_{FB}$ alone [27,28].

TABLE I. Definition of the q^2 bins used in the analysis. The nominal B and K^* invariant masses [29] are given by m_B and m_{K^*}, respectively.

q^2 bin	q^2 min(GeV^2/c^4)	q^2 max(GeV^2/c^4)
q_1^2	0.10	2.00
q_2^2	2.00	4.30
q_3^2	4.30	8.12
q_4^2	10.11	12.89
q_5^2	14.21	$(m_B - m_{K^*})^2$
q_0^2	1.00	6.00

II. EVENT SELECTION

We use a data sample of ∼471 million $B\bar{B}$ pairs, corresponding to $424.2 \pm 1.8\ \mathrm{fb}^{-1}$ [30], collected at the $\Upsilon(4S)$ resonance with the *BABAR*, detector [31] at the PEP-II asymmetric-energy e^+e^- collider at the SLAC National Accelerator Laboratory. Charged particle tracking is provided by a five-layer silicon vertex tracker and a 40-layer drift chamber in a 1.5 T solenoidal magnetic field. We identify electrons and photons with a CsI(Tl) electromagnetic calorimeter, and muons using an instrumented magnetic flux return. We identify charged kaons using a detector of internally reflected Cherenkov light, as well as dE/dx information from the drift chamber. Charged tracks other than identified e, μ and K candidates are treated as pions.

We reconstruct $B \to K^*\ell^+\ell^-$ signal events in the following final states (charge conjugation is implied throughout unless explicitly noted):

(i) $B^+ \to K^{*+}(\to K^0_S\pi^+)\mu^+\mu^-$;
(ii) $B^0 \to K^{*0}(\to K^+\pi^-)\mu^+\mu^-$;
(iii) $B^+ \to K^{*+}(\to K^+\pi^0)e^+e^-$;
(iv) $B^+ \to K^{*+}(\to K^0_S\pi^+)e^+e^-$;
(v) $B^0 \to K^{*0}(\to K^+\pi^-)e^+e^-$.

We do not include the decays $B^+ \to K^{*+}(\to K^+\pi^0)\mu^+\mu^-$ and $B^0 \to K^{*0}(\to K^0_S\pi^0)\ell^+\ell^-$ in our analysis. The expected signal-to-background ratio for these final states relative to the five chosen signal modes listed above is very poor, with ensembles of pseudo-experiments showing that inclusion of these extra modes would yield no additional sensitivity.

We require K^* candidates to have an invariant mass $0.72 < m(K\pi) < 1.10\ \mathrm{GeV}/c^2$. Electron and muon candidates are required to have momenta $p > 0.3\ \mathrm{GeV}/c$ in the laboratory frame. The muon and electron misidentification rates determined from high-purity data control

samples are, respectively, ∼2% and ≲0.1% [31], and backgrounds from particle misidentification are thus significant for $B \to K^* \mu^+ \mu^-$ candidates only. We combine up to three photons with an electron candidate when the photons are consistent with bremsstrahlung from the electron. We do not use electrons that are associated with photon conversions to low-mass e^+e^- pairs. We reconstruct K^0_S candidates in the $\pi^+\pi^-$ final state, requiring an invariant mass consistent with the nominal K^0 mass, and a flight distance from the e^+e^- interaction point that is more than three times the flight distance uncertainty. Neutral pion candidates are formed from two photons with $E_\gamma > 50$ MeV, and an invariant mass between 115 and 155 MeV/c^2. In each final state, we utilize the kinematic variables $m_{\rm ES} = \sqrt{E^2_{\rm CM}/4 - p^{*2}_B}$ and $\Delta E = E^*_B - E_{\rm CM}/2$, where p^*_B and E^*_B are the B momentum and energy in the $\Upsilon(4S)$ center-of-mass (CM) frame, and $E_{\rm CM}$ is the total CM energy. We reject events with $m_{\rm ES} < 5.2$ GeV/c^2.

To characterize backgrounds from hadrons misidentified as muons, we study $K^* h^\pm \mu^\mp$ candidates, where h is a charged track with no particle identification requirement applied. We additionally use a $K^* e^\pm \mu^\mp$ sample, where no signal is expected because of lepton-flavor conservation, to model the combinatorial background from two random leptons. For both e^+e^- and $\mu^+\mu^-$ modes, we veto the $J/\psi(2.85 < m_{\ell^+\ell^-} < 3.18$ GeV/$c^2)$ and $\psi(2S)(3.59 < m_{\ell^+\ell^-} < 3.77$ GeV/$c^2)$ mass regions. These vetoed events provide high-statistics control samples of decays to final states identical to the signal modes here that we use to validate our fitting procedures.

Random combinations of leptons from semileptonic B and D decays are the predominant source of backgrounds. These combinatorial backgrounds occur in both $B\bar{B}$ events ("$B\bar{B}$ backgrounds") and $e^+e^- \to q\bar{q}$ continuum events ("$q\bar{q}$ backgrounds", where $q = u, d, s, c$), and are suppressed using eight bagged decision trees (BDTs) [32] trained for suppression of

(i) $B\bar{B}$ backgrounds in e^+e^- modes at low q^2
(ii) $B\bar{B}$ backgrounds in e^+e^- modes at high q^2
(iii) $B\bar{B}$ backgrounds in $\mu^+\mu^-$ modes at low q^2
(iv) $B\bar{B}$ backgrounds in $\mu^+\mu^-$ modes at high q^2
(v) $q\bar{q}$ backgrounds in e^+e^- modes at low q^2
(vi) $q\bar{q}$ backgrounds in e^+e^- modes at high q^2
(vii) $q\bar{q}$ backgrounds in $\mu^+\mu^-$ modes at low q^2
(viii) $q\bar{q}$ backgrounds in $\mu^+\mu^-$ modes at high q^2,

where low (high) q^2 is defined as the mass-squared region below (above) the vetoed J/ψ region. In order to treat the $K^* e^\pm \mu^\mp$ control sample equivalently to the e^+e^- and $\mu^+\mu^-$ data sets, we similarly train four BDTs for $B\bar{B}$ and $q\bar{q}$ background suppression in the low and high q^2 regions, using a high-statistics sample of simulated $B \to K^* e^\pm \mu^\mp$ events. The $\mu^+\mu^-$ BDTs are used to characterize the $K^* h^\pm \mu^\mp$ data set. We draw our BDT training data sets for both signal and combinatoric backgrounds from simulated events. We find good agreement in the distribution of BDT outputs between simulated events and the charmonium control samples; we find similarly good agreement between data and simulation in the purely combinatoric background off-resonance data.

Each of the above BDTs uses a subset of the following observables as its input parameters:

(i) the B candidate ΔE
(ii) the ratio of Fox-Wolfram moments R_2 [33] and the ratio of the second-to-zeroth angular moments of the energy flow L_2/L_0 [34], both of which are event shape parameters calculated using charged and neutral particles in the CM frame
(iii) the mass and ΔE of the other B meson in the event computed in the laboratory frame by summing the momenta and energies of all charged particles and photons that are not used to reconstruct the signal candidate
(iv) the magnitude of the total transverse momentum of the event
(v) the χ^2 probability of the vertex fitted from all the B candidate tracks
(vi) the cosines of four angles, all defined in the CM frame: the angle between the B candidate momentum and the beam axis, the angle between the event thrust axis and the beam axis, the angle between the thrust axis of the rest of the event and the beam axis, and the angle between the event thrust axis and the thrust axis of the rest of the event. The thrust T of an event comprised of N particles, or analogously for a subset of particles in an event, is defined as [35]

$$T = \frac{\sum_{i=1}^{N} |\vec{p}_i \cdot \hat{t}|}{\sum_{i=1}^{N} |\vec{p}_i|},$$

where the thrust axis $\hat{t}$ maximizes the magnitude of the thrust T, up to a two-fold ambiguity in direction (forward and backward are equivalent).

As an example, Fig. 3 shows histograms of BDT output normalized to unit area for simulated $K^0_S \pi^+ e^+ e^-$ and $K^0_S \pi^+ \mu^+ \mu^-$ signal and combinatorial background events in the q^2_1 bin. The BDT outputs for the other final states and q^2 bins demonstrate similar discriminating power.

Backgrounds from $B \to D(\to K^{(*)}\pi)\pi$ hadronic decays occur if two hadrons are misidentified as leptons, which happens at a non-negligible rate only in dimuon final states. These events are vetoed by requiring the invariant mass of the $K^*\pi$ system to be outside the range $1.84 - 1.90$ GeV/c^2 after assigning the pion mass hypothesis to

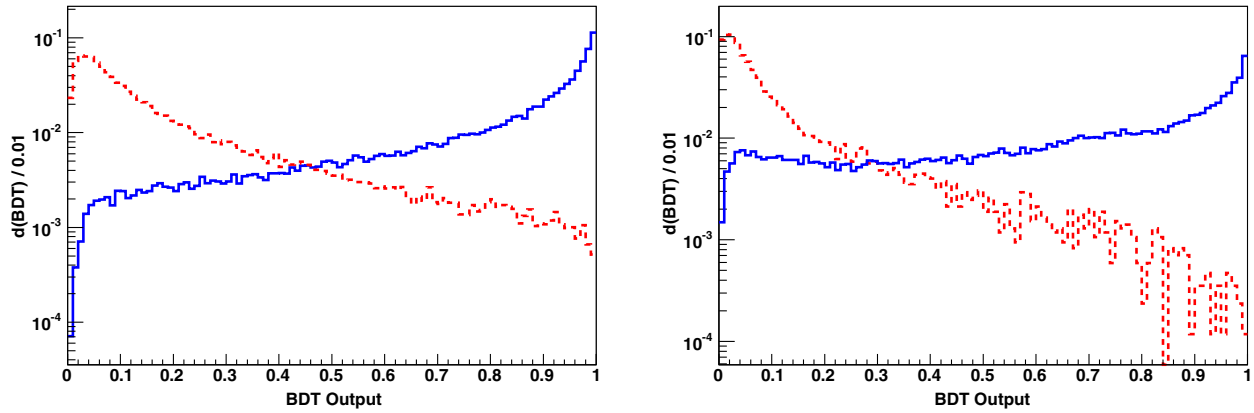

(a) e^+e^- BDT output for $B\overline{B}$ background suppression in $B^+ \to K^0_S\pi^+e^+e^-$.

(b) e^+e^- BDT output for $q\bar{q}$ background suppression in $B^+ \to K^0_S\pi^+e^+e^-$.

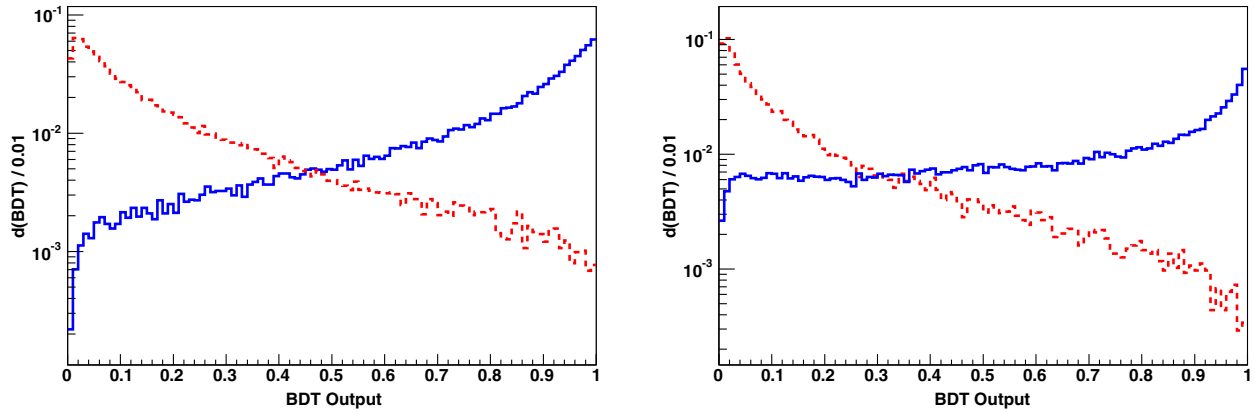

(c) $\mu^+\mu^-$ BDT output for $B\overline{B}$ background suppression in $B^+ \to K^0_S\pi^+\mu^+\mu^-$.

(d) $\mu^+\mu^-$ BDT output for $q\bar{q}$ background suppression in $B^+ \to K^0_S\pi^+\mu^+\mu^-$.

FIG. 3. BDT outputs normalized to unit area for simulated signal (solid blue line) and background (red dashed line) $q^2_{\rm I}$ events.

the muon candidates. Residual muon misidentification backgrounds remaining after this selection are characterized using the $K^*h^\pm\mu^\mp$ data set.

For the last steps in the event selection, we adopt (a) the ΔE regions used in our recent related analyses of rates and rate asymmetries in exclusive $B \to K^{(*)}\ell^+\ell^-$ and inclusive $B \to X_s\ell^+\ell^-$ decays [26,36], $-0.1(-0.05) < \Delta E < 0.05$ GeV for e^+e^- ($\mu^+\mu^-$) modes and (b) the $q\bar{q}$ BDT > 0.4 selection used in the inclusive $B \to X_s\ell^+\ell^-$ analysis [26]. After all other selection criteria have been imposed, this $q\bar{q}$ BDT selection removes ∼70%–90% of $q\bar{q}$ background events, with a concommitant decrease of ∼6%–10% in signal efficiencies.

At the conclusion of the event selection process, some events have multiple reconstructed B candidates which typically differ by one charged or neutral pion in the hadronic system. The signal candidate multiplicity averaged across final states and q^2 bins is ∼1.4 (∼1.1) candidates per event in dielectron (dimuon) modes. In events with multiple signal candidates, the candidate with the ΔE value closest to zero is selected.

III. ANGULAR OBSERVABLES EXTRACTION METHOD

A. General strategy

We extract the angular observables F_L and $\mathcal{A}_{FB}$ from the data using a series of likelihood (LH) fits which proceed in several steps:

(1) In each q^2 bin, for each of the five signal modes separately and using the full $m_{\rm ES} > 5.2$ GeV$/c^2$ data set, an initial unbinned maximum LH fit of $m_{\rm ES}$, $m(K\pi)$ and a likelihood ratio [L_R, defined below in Eq. (3)] that discriminates against random combinatorial $B\bar{B}$ backgrounds is performed. After this first fit, all normalizations and the $m_{\rm ES}$-dependent, $m(K\pi)$-dependent and L_R-dependent probability density function (pdf) shapes are fixed.

(2) Second, in each q^2 bin and for each of the five signal modes separately, $m_{\rm ES}$, $m(K\pi)$ and L_R pdfs and normalizations are defined for $m_{\rm ES} > 5.27$ GeV$/c^2$ events (the "$m_{\rm ES}$ angular fit region") using the results of the prior three-dimensional fits. Only

$m_{\rm ES}$ angular fit region events and pdfs are subsequently used in the fits for F_L and $\mathcal{A}_{FB}$.

(3) Next, $\cos\theta_K$ is added as a fourth dimension to the likelihood function, in addition to $m_{\rm ES}$, $m(K\pi)$ and L_R, and four-dimensional likelihoods with F_L as the only free parameter are defined for $m_{\rm ES}$ angular fit region events. As above, each q^2 bin and each of the five signal modes has its own separate four-dimensional LH function. However, a common value of F_L is shared among all of the four-dimensional LH functions in any given q^2 bin. Thus, by combining LH functions from multiple final states, it becomes possible to extract F_L and $\mathcal{A}_{FB}$ for arbitrary combinations of the five final states here. In particular, we quote results using three different sets of our five signal modes:

(a) $B^+ \to K^{*+}\ell^+\ell^-$, comprised of
  (i) $B^+ \to K^{*+}(\to K^0_S\pi^+)\mu^+\mu^-$,
  (ii) $B^+ \to K^{*+}(\to K^+\pi^0)e^+e^-$,
  (iii) $B^+ \to K^{*+}(\to K^0_S\pi^+)e^+e^-$,

(b) $B^0 \to K^{*0}\ell^+\ell^-$, comprised of
  (i) $B^0 \to K^{*0}(\to K^+\pi^-)\mu^+\mu^-$,
  (ii) $B^0 \to K^{*0}(\to K^+\pi^-)e^+e^-$.

(c) $B \to K^*\ell^+\ell^-$, comprised of
  (i) $B^+ \to K^{*+}(\to K^0_S\pi^+)\mu^+\mu^-$,
  (ii) $B^0 \to K^{*0}(\to K^+\pi^-)\mu^+\mu^-$,
  (iii) $B^+ \to K^{*+}(\to K^+\pi^0)e^+e^-$,
  (iv) $B^+ \to K^{*+}(\to K^0_S\pi^+)e^+e^-$,
  (v) $B^0 \to K^{*0}(\to K^+\pi^-)e^+e^-$.

(4) In the final step, we use the fitted value of F_L from the previous fit step as input to a similar four-dimensional fit for $\mathcal{A}_{FB}$, in which $\cos\theta_\ell$ replaces $\cos\theta_K$ as the fourth dimension in the LH function, in addition to $m_{\rm ES}$, $m(K\pi)$ and L_R.

As mentioned above, we define a likelihood ratio L_R as the third dimension in the initial fit,

$$L_R \equiv \frac{\mathcal{P}_{\rm sig}}{\mathcal{P}_{\rm sig}+\mathcal{P}_{\rm bkg}}, \tag{3}$$

where $\mathcal{P}_{\rm sig}$ and $\mathcal{P}_{\rm bkg}$ are probabilities calculated from the $B\bar{B}$ BDT output for signal and $B\bar{B}$ backgrounds, respectively. $\mathcal{P}_{\rm sig}$ and $\mathcal{P}_{\rm bkg}$ are modeled using several different functional forms depending on q^2 bin and final state. After the multiple candidate selection described at the conclusion of the preceding section and before fitting a data set, a final requirement of $L_R > 0.6$ is made. This drastically reduces the number of background events at the cost of a relatively small loss, dependent on final state and q^2 bin, in signal efficiency. Table II shows final signal efficiencies in the $m_{\rm ES}$ angular fit region for each final state and q^2 bin.

TABLE II. Final signal efficiencies in the $m_{\rm ES}$ angular fit region by mode and q^2 bin.

Mode	q^2_0	q^2_1	q^2_2	q^2_3	q^2_4	q^2_5
$K^0_S\pi^+\mu^+\mu^-$	0.14	0.13	0.15	0.15	0.14	0.11
$K^+\pi^-\mu^+\mu^-$	0.18	0.15	0.19	0.20	0.19	0.16
$K^+\pi^0e^+e^-$	0.12	0.11	0.12	0.12	0.11	0.08
$K^0_S\pi^+e^+e^-$	0.18	0.16	0.19	0.17	0.15	0.11
$K^+\pi^-e^+e^-$	0.23	0.20	0.23	0.23	0.21	0.15

The initial three-dimensional fit is an unbinned maximum likelihood fit with minimization performed by MINUIT [37]. Each angular result is subsequently determined by direct construction and examination of the negative log-likelihood curves resulting from a scan across the entire F_L or $\mathcal{A}_{FB}$ parameter space, including unphysical regions which provide a statistically consistent description of the data.

B. Event classes

We characterize $m_{\rm ES}$, $m(K\pi)$, L_R, $\cos\theta_K$ and $\cos\theta_\ell$ probability density functions in our likelihood fit model for several classes of events:

(i) correctly reconstructed ("true") signal events;
(ii) misreconstructed ("cross-feed") signal events, from both the five signal modes as well as from other $b \to s\ell^+\ell^-$ decays;
(iii) random combinatorial backgrounds;
(iv) backgrounds from J/ψ and $\psi(2S)$ decays which escape the dilepton mass veto windows;
(v) for the $\mu^+\mu^-$ modes only, backgrounds from hadronic decays in which there is muon misidentification of hadrons (this background is negligible in e^+e^- final states due to the much smaller, relative to muons, electron misidentification probability).

1. True and cross-feed signal events

True signal events have all final state daughter particles correctly reconstructed. The true signal normalization for each final state in each q^2 bin is a free parameter in the initial three-dimensional fits. For each final state, the $m_{\rm ES}$ signal pdf is parameterized as a Gaussian with a mean and width fixed to values obtained from a fit to the vetoed J/ψ data events in the same final state. Similarly, for the resonant K^* line shape in each final state, the signal $m(K\pi)$ pdf uses a relativistic Breit-Wigner (BW) with width and pole mass fixed from the vetoed J/ψ data events in the same final state. True signal L_R pdfs for each final state in each q^2 bin are derived from simulated signal events, and are parameterized using histograms. There is good agreement between the L_R shapes derived from simulated events and the L_R shapes observed in the charmonium control sample data.

Equations (1) and (2), showing the dependence of F_L and $\mathcal{A}_{FB}$ on $\cos\theta_K$ and $\cos\theta_\ell$ respectively, are purely theoretical expressions which must be modified to take into account the experimental acceptance. We characterize the angular acceptance using simulated signal events to obtain parameterizations of the $\cos\theta_K$ and $\cos\theta_\ell$ efficiency for each final state in each q^2 bin.

Signal cross feed typically occurs when a low-energy $\pi^\pm$ or π^0 is swapped, added or removed from the set of daughter particles used to reconstruct an otherwise correctly reconstructed signal candidate. There can be self-cross-feed within one signal mode, feed-across between two different signal modes with the same final state particle multiplicity, or (up) down cross feed from (lower) higher multiplicity $s\ell^+\ell^-$ modes. Simulated signal events are used to model these types of decays, with normalization relative to the fitted true signal yield. Averaged over the five signal modes and disjoint q^2 bins $q_1^2 - q_5^2$, the fraction of cross-feed events relative to correctly reconstructed signal decays is $\sim$0.4 for events in the $m_{\rm ES} > 5.27\ {\rm GeV}/c^2$ angular fit region. Generator-level variations in the production of cross-feed events are considered as part of the study of systematic uncertainties related to the modeling of signal decays.

2. Combinatorial backgrounds

The largest source of background is from semileptonic B and D decays, where leptons from two such decays and a K^* candidate combine to form a B candidate. The $m_{\rm ES}$ pdf for the combinatorial background is modeled with a kinematic threshold function [38] whose single shape parameter is a free parameter in the fits. Events in the lepton-flavor violating (LFV) modes $K^*e^\pm\mu^\mp$, which are forbidden in the SM and for which stringent experimental limits exist [29], are reconstructed and selected analogously to the final event selection in order to characterize the combinatorial background $m(K\pi)$ and L_R pdfs. We obtain the angular pdfs for the combinatorial backgrounds in the $m_{\rm ES}$ angular fit region using events in the $m_{\rm ES}$ sideband region $5.2 < m_{\rm ES} < 5.27\ {\rm GeV}/c^2$. The LFV events additionally provide an alternative model for the combinatorial angular pdfs, which is used in the characterization of systematic uncertainties in the angular fits.

3. Charmonium and other physics backgrounds

Some misreconstructed charmonium events escape the charmonium vetoes and appear in our q^2 bins. This typically occurs through bremsstrahlung by electrons, followed by incorrect recovery of the missing energy. The pdfs for this residual charmonium background are modeled using simulated charmonium signal events.

In order to use the vetoed charmonium events as a data control sample, we construct a set of pdfs equivalent to those used in the $B \to K^*\ell^+\ell^-$ angular fits but which are appropriate for J/ψ and $\psi(2S)$ events inside, rather than outside, their respective vetoed mass windows. The BDTs in the low (high) q^2 bin are used to calculate L_R for events within the J/ψ ($\psi(2S)$) mass window.

Gamma conversions from $B \to K^*\gamma$ events and Dalitz decays $(\pi^0, \eta) \to e^+e^-\gamma$ of hadronic B decay daughters give rise to small backgrounds in q_1^2. However, since less than a single event from these sources is expected in the final angular fits, we do not include them in our fit model.

4. Muon misidentification backgrounds

In dimuon modes only, some events pass the final selection but have misidentified hadron(s) taking the place of one or both muon candidates. To model these events, we follow a procedure similar to that described in Ref. [39] by selecting a sample of $K^*\mu^\pm h^\mp$ events requiring that the $\mu^\pm$ candidate be identified as a muon and the $h^\mp$ candidate fail identification as an electron. Using weights obtained from data control samples where a charged particle's species can be identified with high precision and accuracy without using particle identification information, the $K^*\mu^\pm h^\mp$ data set is weighted event-by-event to characterize expected contributions in our fits due to the presence of misidentified muon candidates. The pdfs for these events are implemented as a sum of weighted histograms, with normalizations obtained by construction directly from the weighted control sample data.

C. Initial $m_{\rm ES}$, $m(K\pi)$ and L_R fit

As discussed above, the initial three-dimensional fits to $m_{\rm ES}$, $m(K\pi)$ and L_R are done using events in the full $m_{\rm ES} > 5.2\ {\rm GeV}/c^2$ range; each final state in each q^2 bin is separately fit in order to establish the normalizations and pdf shapes subsequently used in extracting the angular observables from the $m_{\rm ES} > 5.27\ {\rm GeV}/c^2$ angular fit region. Table III gives the resulting fitted signal yields along with statistical uncertainties for the three different combinations of particular final states for which the angular

TABLE III. Fitted signal yields with statistical uncertainties.

Mode	q_0^2	q_1^2	q_2^2	q_3^2	q_4^2	q_5^2
$B \to K^*\ell^+\ell^-$	40.8 ± 8.4	31.7 ± 7.1	11.9 ± 5.5	21.3 ± 8.5	31.9 ± 9.2	33.2 ± 7.8
$B^+ \to K^{*+}\ell^+\ell^-$	17.7 ± 5.2	8.7 ± 4.1	3.8 ± 4.0	7.7 ± 5.6	9.0 ± 4.8	9.4 ± 4.2
$B^0 \to K^{*0}\ell^+\ell^-$	23.1 ± 6.6	22.9 ± 5.8	8.1 ± 3.8	13.7 ± 6.4	22.8 ± 7.8	23.8 ± 6.6

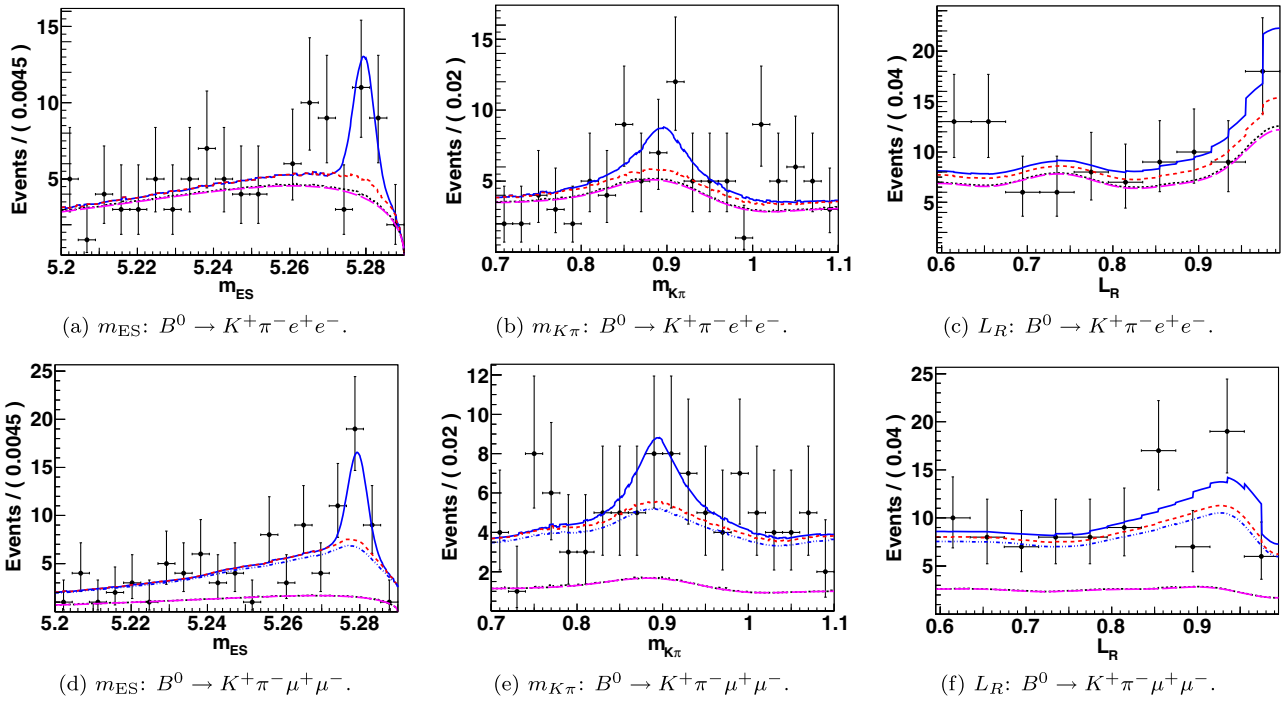

(a) $m_{\rm ES}$: $B^0 \to K^+\pi^- e^+ e^-$. (b) $m_{K\pi}$: $B^0 \to K^+\pi^- e^+ e^-$. (c) L_R: $B^0 \to K^+\pi^- e^+ e^-$.

(d) $m_{\rm ES}$: $B^0 \to K^+\pi^- \mu^+ \mu^-$. (e) $m_{K\pi}$: $B^0 \to K^+\pi^- \mu^+ \mu^-$. (f) L_R: $B^0 \to K^+\pi^- \mu^+ \mu^-$.

FIG. 4. Initial three-dimensional fit projections for $B^0 \to K^+\pi^- e^+ e^-$ (top row) and $B^0 \to K^+\pi^- \mu^+ \mu^-$ (bottom row) in q^2_5. The plots show the stacked contributions from each event class: combinatorial (magenta long dash), charmonium (black dots), cross feed (red short dash), total pdf (solid blue) and, in the bottom row of plots only, muon mis-identification (blue dash dots). The signal pdf is represented by the area between the dash red and solid blue lines.

observables are extracted. As examples of typical fits, Fig. 4 shows fit projections in each of the three initial fit dimensions for $B^0 \to K^+\pi^- e^+ e^-$ and $B^0 \to K^+\pi^- \mu^+ \mu^-$ in the q^2_5 bin. Validation of the initial three-dimensional fit model is done using events in the J/ψ and $\psi(2S)$ dilepton mass veto windows, where we find good agreement between our fit results and the nominal PDG values for the $B \to J/\psi K^*$ and $B \to \psi(2S)K^*$ branching fractions [29] into our final states.

D. Angular fit results

Prior to fitting the $B \to K^*\ell^+\ell^-$ angular data, we validate our angular fit model by using it to extract the K^* longitudinal polarization F_L for $B \to J/\psi K^*$ and $B \to \psi(2S)K^*$ decays into our signal final states, and comparing our results to previously reported PDG values [29]. We also perform similar validation fits for $\mathcal{A}_{FB}$, which is expected in the SM to approach zero for lepton pairs from B decays to final states including charmonia. Recalculating the PDG averages after removing all contributing *BABAR*, results, we find no significant deviations from the expected values in any individual final state or for the particular combinations of final states used in our main analysis.

Having validated our fit model with the vetoed charmonium events, we proceed to the extraction of the angular observables in each q^2 bin. Our results are tabulated in Tables IV and V; Figs. 5 and 6 show the $B^+ \to K^{*+}\ell^+\ell^-$ and $B^0 \to K^{*0}\ell^+\ell^-$ $\cos\theta_K$ and $\cos\theta_\ell$ fit projections in q^2_0

TABLE IV. F_L angular fit results with, respectively, statistical and systematic uncertainties.

	$B^+ \to K^{*+}\ell^+\ell^-$	$B^0 \to K^{*0}\ell^+\ell^-$	$B \to K^*\ell^+\ell^-$
q^2_0	$+0.05^{+0.09+0.02}_{-0.10-0.10}$	$+0.43^{+0.12+0.02}_{-0.13-0.02}$	$+0.24^{+0.09+0.02}_{-0.08-0.02}$
q^2_1	$-0.02^{+0.18+0.09}_{-0.13-0.14}$	$+0.34^{+0.15+0.15}_{-0.10-0.02}$	$+0.29^{+0.09+0.13}_{-0.12-0.05}$
q^2_2	$-0.24^{+0.27+0.18}_{-0.39-0.10}$	$+0.18^{+0.16+0.02}_{-0.12-0.10}$	$+0.17^{+0.14+0.02}_{-0.15-0.02}$
q^2_3	$+0.15^{+0.14+0.05}_{-0.13-0.08}$	$+0.48^{+0.14+0.05}_{-0.16-0.05}$	$+0.30^{+0.12+0.05}_{-0.11-0.07}$
q^2_4	$+0.05^{+0.27+0.16}_{-0.16-0.15}$	$+0.45^{+0.09+0.06}_{-0.14-0.06}$	$+0.34^{+0.15+0.07}_{-0.10-0.10}$
q^2_5	$+0.72^{+0.20+0.10}_{-0.31-0.21}$	$+0.48^{+0.12+0.02}_{-0.12-0.11}$	$+0.53^{+0.10+0.07}_{-0.12-0.14}$

TABLE V. $\mathcal{A}_{FB}$ angular fit results with, respectively, statistical and systematic uncertainties.

	$B^+ \to K^{*+}\ell^+\ell^-$	$B^0 \to K^{*0}\ell^+\ell^-$	$B \to K^*\ell^+\ell^-$
q^2_0	$+0.32^{+0.18+0.08}_{-0.18-0.05}$	$+0.06^{+0.15+0.06}_{-0.18-0.05}$	$+0.21^{+0.10+0.07}_{-0.15-0.09}$
q^2_1	$+0.44^{+0.20+0.13}_{-0.22-0.16}$	$-0.12^{+0.23+0.10}_{-0.21-0.21}$	$+0.10^{+0.16+0.08}_{-0.15-0.19}$
q^2_2	$+0.70^{+0.21+0.36}_{-0.38-0.49}$	$+0.33^{+0.21+0.12}_{-0.30-0.11}$	$+0.44^{+0.15+0.14}_{-0.18-0.11}$
q^2_3	$+0.11^{+0.22+0.08}_{-0.28-0.20}$	$+0.17^{+0.14+0.08}_{-0.16-0.08}$	$+0.15^{+0.14+0.08}_{-0.12-0.05}$
q^2_4	$+0.21^{+0.32+0.11}_{-0.33-0.24}$	$+0.40^{+0.12+0.17}_{-0.18-0.16}$	$+0.42^{+0.11+0.14}_{-0.17-0.13}$
q^2_5	$+0.40^{+0.26+0.18}_{-0.21-0.17}$	$+0.29^{+0.14+0.10}_{-0.17-0.10}$	$+0.29^{+0.07+0.10}_{-0.10-0.12}$

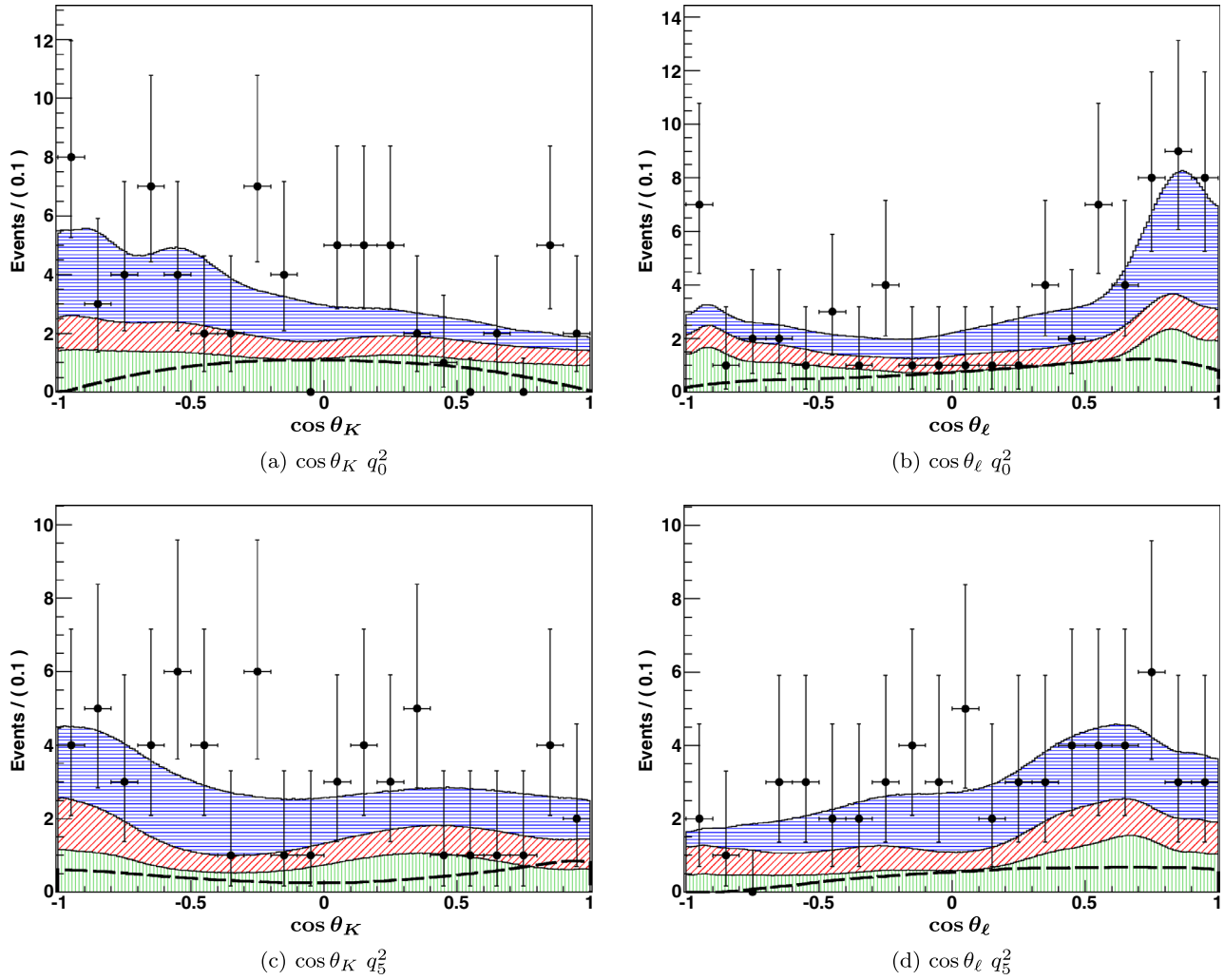

(a) $\cos\theta_K$ q_0^2 (b) $\cos\theta_\ell$ q_0^2

(c) $\cos\theta_K$ q_5^2 (d) $\cos\theta_\ell$ q_5^2

FIG. 5. $B^+ \to K^{*+}\ell^+\ell^-$ angular fit projections. The shaded areas show the contribution to the total fit from each individual final state: (green vertical lines) $B^+ \to K_S^0\pi^+\mu^+\mu^-$; (red diagonal lines) $B^+ \to K_S^0\pi^+e^+e^-$; (blue horizontal lines) $B^+ \to K^+\pi^0e^+e^-$. The overlaid dashed line shows the total signal contribution summed over the three individual final states. Each colored band includes both signal and background events in a given final state.

and q_5^2. Figure 7 graphically shows our F_L and $\mathcal{A}_{FB}$ results in disjoint q^2 bins alongside other published results and the SM theory expectations, the latter of which typically have 5%–10% theory uncertainties (absolute) in the regions below and above the charmonium resonances. Figure 8 similarly compares the q_0^2 results obtained here with those of other experiments and the SM theory expectation.

E. Systematic uncertainties

We describe below the systematic uncertainties in the angular results arising from

(i) the purely statistical uncertainties in the parameters obtained from the initial three-dimensional $m_{\rm ES}, m(K\pi)$ fit which are used in the angular fits,
(ii) the F_L statistical uncertainty, which is propagated into the $\mathcal{A}_{FB}$ fit, and
(iii) the modeling of the random combinatorial background pdfs and the signal angular efficiencies.

We additionally examined several other possible sources of systematic uncertainty, but found no significant contributions due to

(i) modeling of the signal cross-feed contributions to the angular fits
(ii) the parameterization of the signal Gaussian $m_{\rm ES}$ and resonant $m(K\pi)$ shapes that are extracted from the relatively high-statistics J/ψ control samples
(iii) possible fit biases which, to relatively very good precision, were not observed in any of the data control sample angular fits
(iv) characterization of $m_{\rm ES}$ peaking backgrounds from muon mis-identification and charmonium leakage;
(v) variations in event selection.

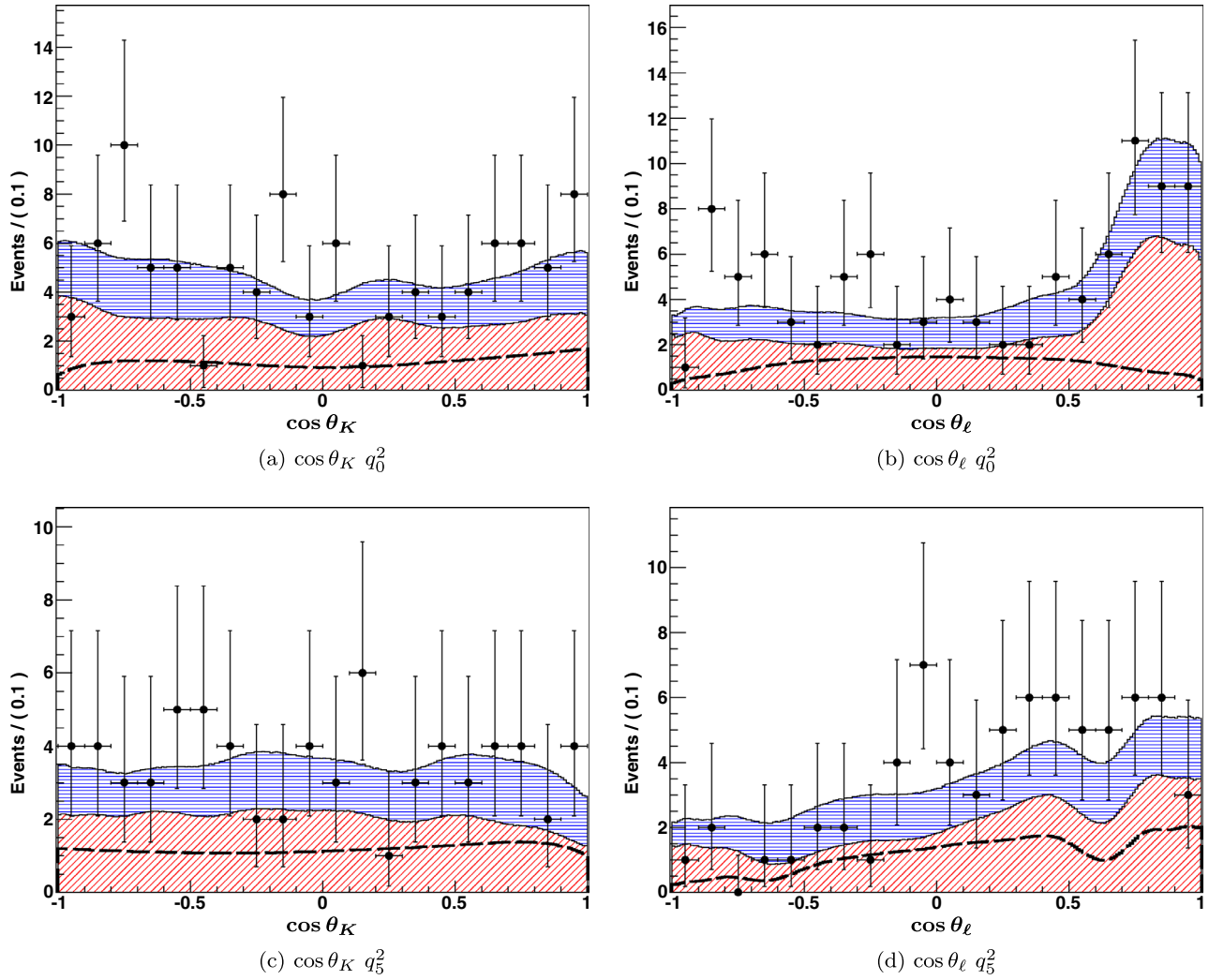

(a) $\cos\theta_K$ q_0^2 (b) $\cos\theta_\ell$ q_0^2

(c) $\cos\theta_K$ q_5^2 (d) $\cos\theta_\ell$ q_5^2

FIG. 6. $B^0 \to K^{*0}\ell^+\ell^-$ angular fit projections. The shaded areas show the contribution to the total fit from each individual final state: (red diagonal lines) $B^0 \to K^+\pi^-\mu^+\mu^-$; (blue horizontal lines) $B^0 \to K^+\pi^-e^+e^-$. The overlaid dashed line shows the total signal contribution summed over the two individual final states. Each colored band includes both signal and background events in a given final state.

We combine in quadrature the individual systematic uncertainties to obtain the total systematic uncertainty on each of the angular observables; these are given in Table X, which is placed after the detailed discussion below for each family of systematic uncertainties.

In the initial fits that determine the signal yields, we allow the random combinatorial $m_{\rm ES}$ shape and normalisation, as well as the signal yield, to float. We then fix these parameters at their central values for the angular fits. To study the systematic uncertainty associated with these fixed parameters, we vary each parameter from its central value by its $\pm 1\sigma$ statistical uncertainty, accounting for correlations among the fit parameters, and then redo the angular fit. To control for systematic fit results that deviate from the nominal central value mainly from statistical effects rather than systematic ones, we additionally examine fit results obtained from $\pm(0.8, 0.9, 1.1, 1.2)\sigma$ variations. These small variations on the $\pm 1\sigma$ values should also result in similarly small variations, in the absence of any statistical effects, on a $\pm 1\sigma$ systematic fit result. For the bulk of the systematics, where the series of fit results for each of the additional variations is linearly distributed around the middle 1σ fit result, the 1σ variation is considered robust. In the relatively few cases where the disagreement between the nominal 1σ variation and the value of the 1σ variation interpolated from the additional $(0.8, 0.9, 1.1, 1.2)\sigma$ variations is statistically significant, the interpolated 1σ value is used to assign the systematic. All deviations from the nominal fit central value are then added in quadrature to obtain the overall systematic uncertainty attributable to this source, which is given in Table VI.

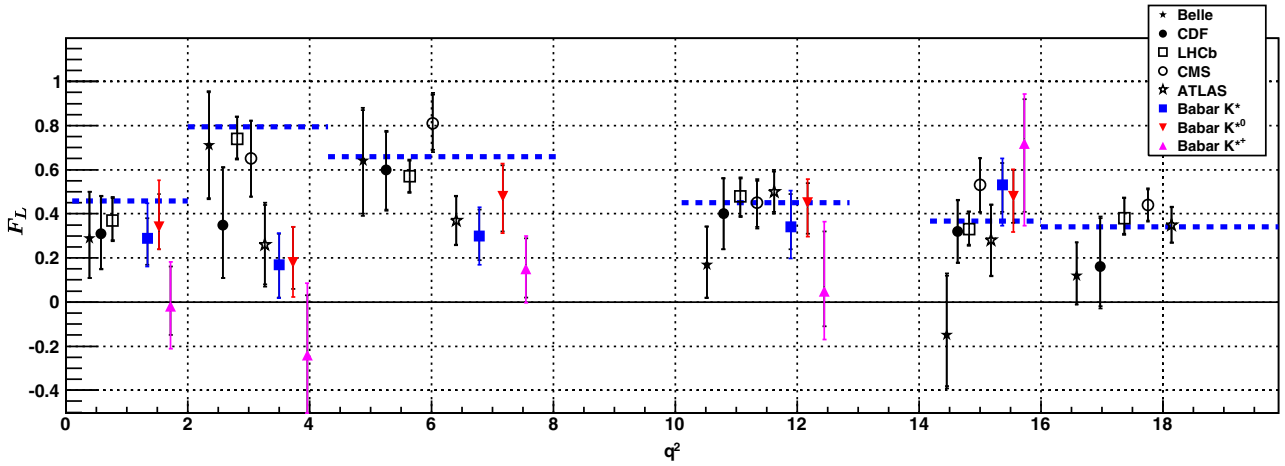

(a) F_L.

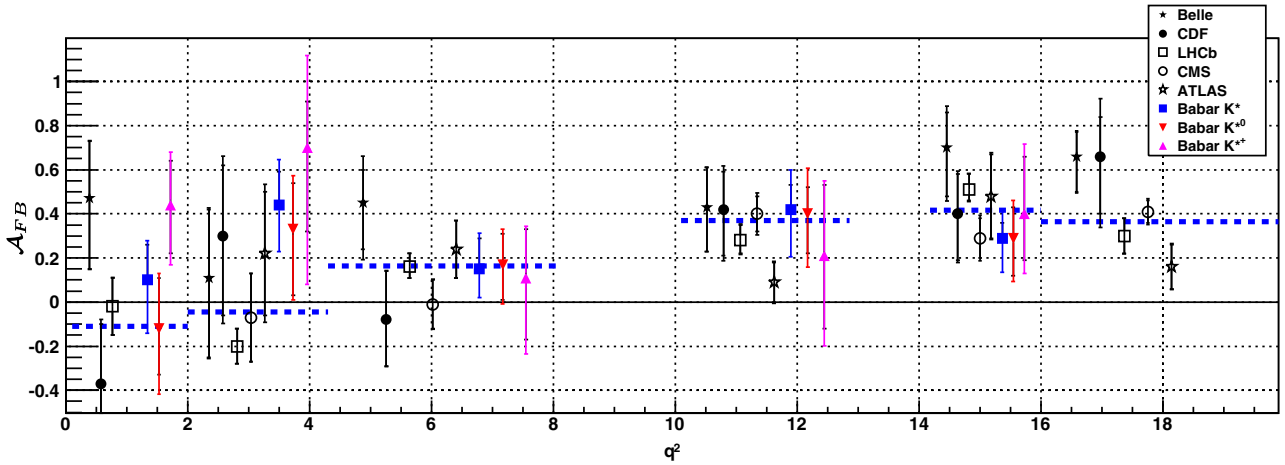

(b) $\mathcal{A}_{FB}$.

FIG. 7. F_L (top) and $\mathcal{A}_{FB}$ (bottom) results in disjoint q^2 bins, along with those of other experiments and the SM expectations (blue dashed lines, which also define the extent of each individual q^2 bin): (black filled star) Belle [19], (black filled circle) CDF [20], (black open square) LHCb [21], (black open circle) CMS [22], (black open star) ATLAS [23], (blue filled square) *BABAR*, $B \to K^* \ell^+ \ell^-$, (red filled down-pointing triangle) $B^0 \to K^{*0} \ell^+ \ell^-$, (magenta filled up-pointing triangle) $B^+ \to K^{*+} \ell^+ \ell^-$. The *BABAR*, q_5^2 results are drawn in the $14 \lesssim q^2 < 16$ GeV$^2/c^4$ region; however, they are valid for the entire $q2 \gtrsim 14$ GeV$^2/c^4$ region.

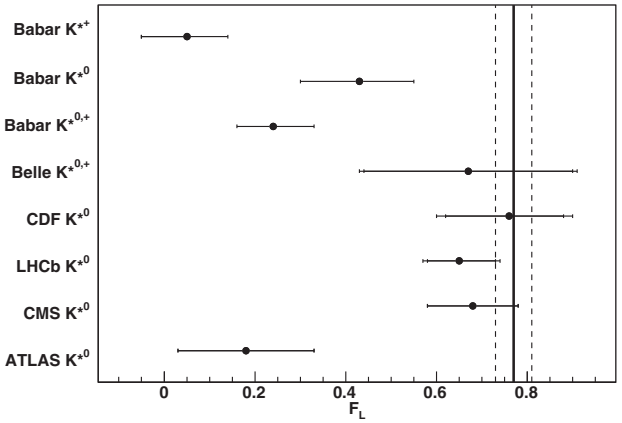

(a) F_L.

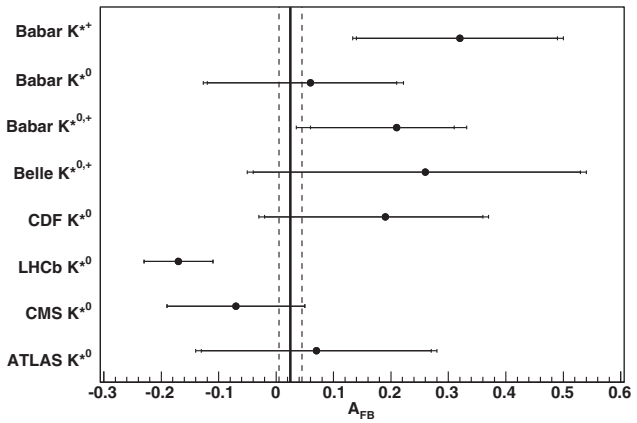

(b) $\mathcal{A}_{FB}$.

FIG. 8. q_0^2 F_L (left) and $\mathcal{A}_{FB}$ (right) results, along with those of other experiments [19–23] and the SM expectation (vertical lines) [1–5,7].

TABLE VI. Angular observable systematic uncertainties from the initial three-dimensional fit.

	F_L systematic			$\mathcal{A}_{FB}$ systematic		
	$B^+ \to K^{*+}\ell^+\ell^-$	$B^0 \to K^{*0}\ell^+\ell^-$	$B \to K^*\ell^+\ell^-$	$B^+ \to K^{*+}\ell^+\ell^-$	$B^0 \to K^{*0}\ell^+\ell^-$	$B \to K^*\ell^+\ell^-$
q_0^2	$+0.02-0.09$	$+0.02-0.02$	$+0.02-0.02$	$+0.05-0.04$	$+0.01-0.04$	$+0.02-0.07$
q_1^2	$+0.09-0.13$	$+0.02-0.02$	$+0.02-0.05$	$+0.12-0.08$	$+0.07-0.02$	$+0.07-0.08$
q_2^2	$+0.18-0.05$	$+0.02-0.01$	$+0.02-0.02$	$+0.34-0.48$	$-0.02-0.08$	$+0.09-0.07$
q_3^2	$+0.05-0.07$	$+0.02-0.02$	$+0.05-0.06$	$+0.02-0.19$	$-0.02-0.04$	$+0.01-0.02$
q_4^2	$+0.11-0.14$	$+0.02-0.06$	$+0.02-0.10$	$+0.09-0.23$	$+0.15-0.11$	$+0.13-0.10$
q_5^2	$+0.02-0.19$	$+0.02-0.10$	$+0.02-0.14$	$+0.16-0.09$	$+0.05-0.02$	$+0.08-0.02$

The $\cos\theta_K$ fit yields the central value and statistical uncertainty for F_L in each q^2 bin, which is subsequently used in the fit to the $\cos\theta_\ell$ distributions to extract $\mathcal{A}_{FB}$. To study the systematic uncertainty on $\mathcal{A}_{FB}$ due to the purely statistical F_L uncertainty, we vary the value of F_L by $\pm 1\sigma$ from its fitted value, and redo the $\cos\theta_\ell$ fits with the new value of F_L. We determine the systematic uncertainty from the shift in the central value of $\mathcal{A}_{FB}$ relative to the nominal fit for $\pm 1\sigma$ variations of F_L; these are given in Table VII. As with the variations described in the preceding paragraph, additional fits for several F_L variations surrounding the nominal $\pm 1\sigma$ values are performed. We then apply the same quality criterion as for the preceding systematic and, where this criterion is not met, assign the F_L systematic using an interpolated 1σ value rather than the fitted 1σ variation.

TABLE VII. Systematic uncertainty in $\mathcal{A}_{FB}$ from the experimental determination of F_L.

	$\mathcal{A}_{FB}$ systematic		
	$B^+ \to K^{*+}\ell^+\ell^-$	$B^0 \to K^{*0}\ell^+\ell^-$	$B \to K^*\ell^+\ell^-$
q_0^2	± 0.04	± 0.04	± 0.04
q_1^2	± 0.04	± 0.07	± 0.04
q_2^2	± 0.07	± 0.07	± 0.08
q_3^2	± 0.03	± 0.06	± 0.04
q_4^2	± 0.04	± 0.07	± 0.06
q_5^2	± 0.08	± 0.07	± 0.07

The angular combinatorial background shapes are derived from the $m_{\rm ES}$ sideband region and are nonparametrically modeled directly from these data. We examine several variations on the modeling, and additionally use the LFV events (described above) as an alternative data set from which the angular background pdfs are drawn. We assign a systematic uncertainty associated with the modeling of these pdfs by using 20 different variations of the nonparametric modeling and refitting for F_L and $\mathcal{A}_{FB}$. We take the largest of the deviations between the default nominal fit and these varied fit results, and to this add in quadrature the deviation from the nominal fit obtained using the LFV data set; the resulting systematic uncertainty is given in Table VIII.

Finally, to study a possible systematic uncertainty on F_L and $\mathcal{A}_{FB}$ as a function of their true physical values, we generated and reconstructed simulated events with varied values of the underlying Wilson coefficients C_7, C_9, and C_{10} in order to produce a range of near-maximal, but physically allowed, asymmetries. These data sets are used to produce signal efficiency histograms differing from the default ones, which use the expected SM values for the Wilson coefficients. This allows different regions of the angular distributions to contribute with different relative weight depending on the magnitude and sign of the underlying angular asymmetries. Applying these alternative signal efficiency histograms, we measure the shifts in the fitted values of F_L and $\mathcal{A}_{FB}$, and assign as the systematic the sum-in-quadrature of each deviation from

TABLE VIII. Systematic uncertainties from combinatorial background modeling. "—" denotes where there is no uncertainty associated with a particular systematic.

	F_L systematic			$\mathcal{A}_{FB}$ systematic		
	$B^+ \to K^{*+}\ell^+\ell^-$	$B^0 \to K^{*0}\ell^+\ell^-$	$B \to K^*\ell^+\ell^-$	$B^+ \to K^{*+}\ell^+\ell^-$	$B^0 \to K^{*0}\ell^+\ell^-$	$B \to K^*\ell^+\ell^-$
q_0^2	— -0.05	— —	— —	$+0.04$ —	— —	— -0.04
q_1^2	$+0.02-0.02$	— —	— —	$+0.05$ —	— —	— —
q_2^2	— -0.05	— —	— —	— -0.07	— -0.04	— —
q_3^2	— —	— —	— —	— —	— —	— —
q_4^2	$+0.10$ —	— —	— —	— -0.04	— —	— —
q_5^2	— -0.10	— -0.05	— —	$+0.04-0.08$	$+0.04$ —	— —

TABLE IX. Systematic uncertainties from signal angular efficiency modeling. "—" denotes where there is no uncertainty associated with a particular systematic.

	F_L systematic			$\mathcal{A}_{FB}$ systematic		
	$B^+ \to K^{*+}\ell^+\ell^-$	$B^0 \to K^{*0}\ell^+\ell^-$	$B \to K^*\ell^+\ell^-$	$B^+ \to K^{*+}\ell^+\ell^-$	$B^0 \to K^{*0}\ell^+\ell^-$	$B \to K^*\ell^+\ell^-$
q_0^2	— −0.02	— —	— —	+0.04 —	+0.04 —	+0.05 —
q_1^2	+0.02 − 0.04	+0.14 —	+0.13 —	— −0.13	— −0.20	— −0.17
q_2^2	— −0.07	— −0.10	— −0.02	+0.12 —	+0.09 —	+0.07 —
q_3^2	— −0.04	+0.04 − 0.05	+0.02 − 0.04	+0.08 —	+0.06 − 0.04	+0.07 − 0.02
q_4^2	+0.07 − 0.05	+0.06 —	+0.07 —	+0.06 —	— −0.09	+0.02 − 0.06
q_5^2	+0.10 —	+0.02 —	+0.07 —	— −0.09	— −0.08	— −0.10

TABLE X. Total systematic uncertainties.

	F_L systematic			$\mathcal{A}_{FB}$ systematic		
	$B^+ \to K^{*+}\ell^+\ell^-$	$B^0 \to K^{*0}\ell^+\ell^-$	$B \to K^*\ell^+\ell^-$	$B^+ \to K^{*+}\ell^+\ell^-$	$B^0 \to K^{*0}\ell^+\ell^-$	$B \to K^*\ell^+\ell^-$
q_0^2	+0.02 − 0.10	+0.02 − 0.02	+0.02 − 0.02	+0.08 − 0.05	+0.06 − 0.05	+0.07 − 0.09
q_1^2	+0.09 − 0.14	+0.15 − 0.02	+0.13 − 0.05	+0.13 − 0.16	+0.10 − 0.21	+0.08 − 0.19
q_2^2	+0.18 − 0.10	+0.02 − 0.10	+0.02 − 0.02	+0.36 − 0.49	+0.12 − 0.11	+0.14 − 0.11
q_3^2	+0.05 − 0.08	+0.05 − 0.05	+0.05 − 0.07	+0.08 − 0.20	+0.08 − 0.08	+0.08 − 0.05
q_4^2	+0.16 − 0.15	+0.06 − 0.06	+0.07 − 0.10	+0.11 − 0.24	+0.17 − 0.16	+0.14 − 0.13
q_5^2	+0.10 − 0.21	+0.02 − 0.11	+0.07 − 0.14	+0.18 − 0.17	+0.10 − 0.10	+0.10 − 0.12

the nominal central value; the resulting systematic uncertainty is shown in Table IX.

F. Extraction of P_2 from the angular fit results

As mentioned above in the Introduction, F_L and $\mathcal{A}_{FB}$ can be used to parameterize an additional angular observable, $P_2 = (-2/3) * \mathcal{A}_{FB}/(1 - F_L)$, which has diminished theory uncertainty and greater sensitivity to non-SM contributions than either F_L or $\mathcal{A}_{FB}$ alone [27,28]. Table XI gives our results for P_2. The 68% confidence intervals quoted are frequentist and derived from ensembles of fits to simulated data sets randomly drawn from the correlated confidence-level contours for F_L and $\mathcal{A}_{FB}$. For the disjoint mass-squared bins q_1^2 to q_5^2, Fig. 9 graphically shows our results overlaid on the SM expectations from theory (as given in Table 3 (KMPW) of Ref. [28]) in the mass-squared region below the J/ψ. In the q_0^2 mass-squared bin, the SM expectation (from the same source) for P_2 is 0.11 ± 0.10, in slight tension with our experimental result.

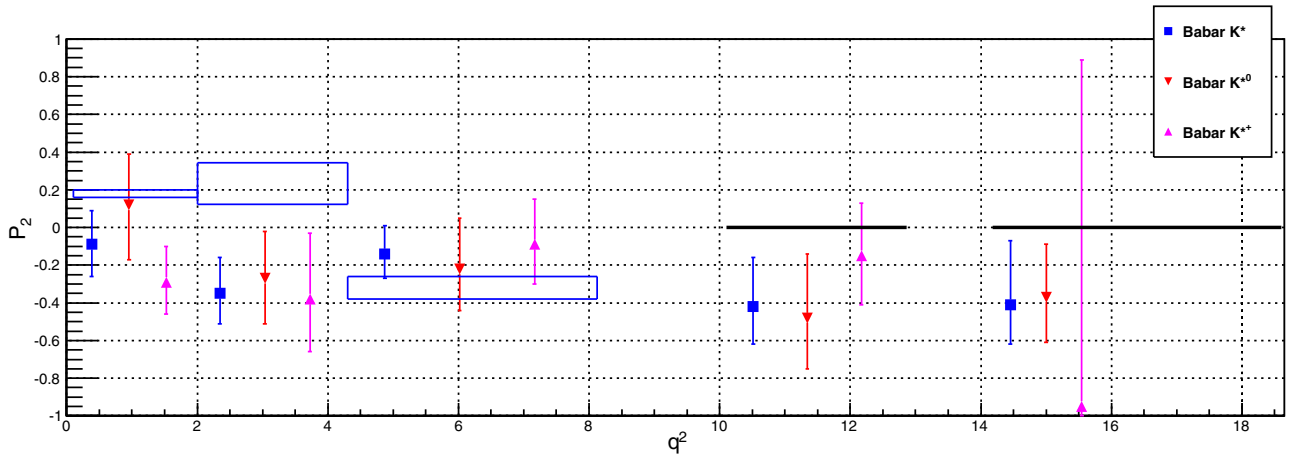

FIG. 9. P_2 results with total uncertainties.The blue boxes show the SM theory expectation in the low mass-squared region; there are no comparable calculations in the high mass-squared region, where the black lines simply denote the extent of the q_4^2 and q_5^2 bins.

TABLE XI. P_2 results with total uncertainties.

	$B^+ \to K^{*+}\ell^+\ell^-$	$B^0 \to K^{*0}\ell^+\ell^-$	$B \to K^*\ell^+\ell^-$
q_0^2	$-0.22^{+0.14}_{-0.13}$	$-0.07^{+0.20}_{-0.21}$	$-0.18^{+0.13}_{-0.13}$
q_1^2	$-0.29^{+0.19}_{-0.17}$	$+0.12^{+0.27}_{-0.29}$	$-0.09^{+0.18}_{-0.17}$
q_2^2	$-0.38^{+0.35}_{-0.28}$	$-0.27^{+0.25}_{-0.24}$	$-0.35^{+0.19}_{-0.16}$
q_3^2	$-0.09^{+0.24}_{-0.21}$	$-0.22^{+0.27}_{-0.22}$	$-0.14^{+0.15}_{-0.13}$
q_4^2	$-0.15^{+0.28}_{-0.26}$	$-0.48^{+0.34}_{-0.27}$	$-0.42^{+0.26}_{-0.20}$
q_5^2	$-0.95^{+1.84}_{-0.96}$	$-0.37^{+0.28}_{-0.24}$	$-0.41^{+0.34}_{-0.21}$

IV. CONCLUSION

In conclusion, we have measured in bins of dilepton mass-squared the fraction F_L of longitudinally polarized K^* decays and the lepton forward-backward asymmetry $\mathcal{A}_{FB}$ in the decays $B^+ \to K^{*+}\ell^+\ell^-$, $B^0 \to K^{*0}\ell^+\ell^-$ and $B \to K^*\ell^+\ell^-$. Results for the $B^+ \to K^{*+}\ell^+\ell^-$ final state are presented for the first time here. Figure 7 graphically shows our F_L and $\mathcal{A}_{FB}$ results in disjoint q^2 bins alongside other published results and the SM theory expectations, the latter of which typically have 5%–10% theory uncertainties in the regions below and above the charmonium resonances. Figure 8 similarly compares the q_0^2 results obtained here with those of other experiments and the SM theory expectation.

As shown in these figures, our $B^0 \to K^{*0}\ell^+\ell^-$ results are in reasonable agreement with both SM theory expectations and other experimental results. Similarly, although with relatively larger uncertainties, we observe broad agreement of the $B^+ \to K^{*+}\ell^+\ell^-$ results with those for $B^0 \to K^{*0}\ell^+\ell^-$. However, in the low dilepton mass-squared region, we observe relatively very small values for F_L in $B^+ \to K^{*+}\ell^+\ell^-$, exhibiting tension with both the $B^0 \to K^{*0}\ell^+\ell^-$ results as well as the SM expectations. These tensions in F_L are difficult to interpret because of uncertainties due to form-factor contributions in the calculation of this observable in both the SM and NP scenarios. However, as shown in Fig. 9 in the same mass-squared region, there is also tension between the experimental results and the expected SM value for P_2, an observable explicitly constructed to minimize such uncertainties. In particular, our P_2 results in q_2^2 are consistent with the existence of substantial right-hand current contributions [40].

ACKNOWLEDGMENTS

We would like to express our gratitude to Joaquim Matias for discussions regarding the observable P_2. We are grateful for the extraordinary contributions of our PEP-II colleagues in achieving the excellent luminosity and machine conditions that have made this work possible. The success of this project also relies critically on the expertise and dedication of the computing organizations that support *BABAR*. The collaborating institutions wish to thank SLAC for its support and the kind hospitality extended to them. This work is supported by the U.S. Department of Energy and the National Science Foundation, the Natural Sciences and Engineering Research Council (Canada), the Commissariat à l'Energie Atomique and Institut National de Physique Nucléaire et de Physique des Particules (France), the Bundesministerium für Bildung und Forschung and Deutsche Forschungsgemeinschaft (Germany), the Istituto Nazionale di Fisica Nucleare (Italy), the Foundation for Fundamental Research on Matter (The Netherlands), the Research Council of Norway, the Ministry of Education and Science of the Russian Federation, Ministerio de Economía y Competitividad (Spain), the Science and Technology Facilities Council (United Kingdom), and the Binational Science Foundation (U.S.-Israel). Individuals have received support from the Marie-Curie IEF program (European Union) and the A. P. Sloan Foundation (USA).

[1] G. Buchalla, A. J. Buras, and M. E. Lautenbacher, Rev. Mod. Phys. **68**, 1125 (1996).
[2] W. Altmannshofer, P. Ball, A. Bharucha, A. J. Buras, D. M. Straub, and M. Wick, J. High Energy Phys. 01 (2009) 019.
[3] F. Kruger, L. M. Sehgal, N. Sinha, and R. Sinha, Phys. Rev. D **61**, 114028 (2000); **63**, 019901(E) (2000).
[4] A. Ali, E. Lunghi, C. Greub, and G. Hiller, Phys. Rev. D **66**, 034002 (2002).
[5] K. S. M. Lee, Z. Ligeti, I. W. Stewart, and F. J. Tackmann, Phys. Rev. D **75**, 034016 (2007).
[6] F. Kruger and J. Matias, Phys. Rev. D **71**, 094009 (2005).
[7] A. Hovhannisyan, W. S. Hou, and N. Mahajan, Phys. Rev. D **77**, 014016 (2008).
[8] G. Burdman, Phys. Rev. D **52**, 6400 (1995).
[9] J. L. Hewett and J. D. Wells, Phys. Rev. D **55**, 5549 (1997).
[10] A. Ali, P. Ball, L. T. Handoko, and G. Hiller, Phys. Rev. D **61**, 074024 (2000).
[11] Q.-S. Yan, C.-S. Huang, W. Liao, and S.-H. Zhu, Phys. Rev. D **62**, 094023 (2000).
[12] T. Feldmann and J. Matias, J. High Energy Phys. 01 (2003) 074.
[13] W. J. Li, Y. B. Dai, and C. S. Huang, Eur. Phys. J. C **40**, 565 (2005).

[14] Y. G. Xu, R. M. Wang, and Y. D. Yang, Phys. Rev. D **74**, 114019 (2006).
[15] P. Colangelo, F. De Fazio, R. Ferrandes, and T. N. Pham, Phys. Rev. D **73**, 115006 (2006).
[16] A. K. Alok, A. Datta, A. Dighe, M. Duraisamy, D. Ghosh, and D. London, J. High Energy Phys. 11 (2011) 121.
[17] A. K. Alok, A. Datta, A. Dighe, M. Duraisamy, D. Ghosh, and D. London, J. High Energy Phys. 11 (2011) 122.
[18] B. Aubert *et al.* (*BABAR*, Collaboration), Phys. Rev. D **79**, 031102 (2009).
[19] J.-T. Wei *et al.* (Belle Collaboration), Phys. Rev. Lett. **103**, 171801 (2009).
[20] T. Aaltonen *et al.* (CDF Collaboration), Phys. Rev. Lett. **108**, 081807 (2012).
[21] R. Aaij *et al.* (LHCb Collaboration), J. High Energy Phys. 08 (2013) 131.
[22] S. Chatrchyan *et al.* (CMS Collaboration), Phys. Lett. B **727**, 77 (2013).
[23] G. Aad *et al.* (ATLAS Collaboration), Report No. ATLAS-CONF-2013-038.
[24] R. Aaij *et al.* (LHCb Collaboration), Phys. Rev. Lett. **111**, 191801 (2013); J. High Energy Phys. 02 (2016) 104.
[25] A. J. Buras and J. Girrbach, J. High Energy Phys. 12 (2013) 009; S. Jäger and J. Martin Camalich, J. High Energy Phys. 05 (2013) 043; W. Altmannshofer and D. M. Straub, Eur. Phys. J. C **73**, 2646 (2013); R. Gauld, F. Goertz, and U. Haisch, Phys. Rev. D **89**, 015005 (2014); J. High Energy Phys. 01 (2014) 069; F. Beaujean, C. Bobeth, and D. van Dyk, Eur. Phys. J. C **74**, 2897 (2014); **74**, 3179(E) (2014); R. R. Horgan, Z. Liu, S. Meinel, and M. Wingate, Phys. Rev. Lett. **112**, 212003 (2014); A. J. Buras, F. De Fazio, and J. Girrbach, J. High Energy Phys. 02 (2014) 112; T. Hurth and F. Mahmoudi, J. High Energy Phys. 04 (2014) 097.
[26] J. P. Lees *et al.* (*BABAR*, Collaboration), Phys. Rev. Lett. **112**, 211802 (2014).
[27] D. Becirevic and E. Schneider, Nucl. Phys. **B854**, 321 (2012); J. Matias, F. Mescia, M. Ramon, and J. Virto, J. High Energy Phys. 04 (2012) 104; S. Descotes-Genon, J. Matias, and J. Virto, Phys. Rev. D **88**, 074002 (2013); S. Descotes-Genon, T. Hurth, J. Matias, and J. Virto, J. High Energy Phys. 05 (2013) 137; S. Descotes-Genon, J. Matias, M. Ramon, and J. Virto, J. High Energy Phys. 01 (2013) 048.
[28] S. Descotes-Genon, L. Hofer, J. Matias, and J. Virto, J. High Energy Phys. 12 (2014) 125.
[29] K. A. Olive (Particle Data Group), Chin. Phys. C **38**, 090001 (2014).
[30] J. P. Lees *et al.* (*BABAR*, Collaboration), Nucl. Instrum. Methods Phys. Res., Sect. A **726**, 203 (2013).
[31] B. Aubert *et al.* (*BABAR*, Collaboration), Nucl. Instrum. Methods Phys. Res., Sect. A **479**, 1 (2002); Nucl. Instrum. Methods Phys. Res., Sect. A **729**, 615 (2013).
[32] L. Breiman, Mach. Learn. **24**, 123 (1996); I. Narsky, arXiv: physics/0507157 (2005).
[33] G. C. Fox and S. Wolfram, Phys. Rev. Lett. **41**, 1581 (1978).
[34] B. Aubert *et al.* (*BABAR*, Collaboration), Phys. Rev. Lett. **89**, 281802 (2002).
[35] S. Brandt and H. D. Dahmen, Z. Phys. C **1**, 61 (1979).
[36] J. P. Lees *et al.* (*BABAR*, Collaboration), Phys. Rev. D **86**, 032012 (2012).
[37] F. James and M. Roos, Comput. Phys. Commun. **10**, 343 (1975); W. Verkerke and D. P. Kirkby, eConf C **0303241**, MOLT007 (2003).
[38] H. Albrecht *et al.* (ARGUS Collaboration), Z. Phys. C **48**, 543 (1990).
[39] B. Aubert *et al.* (*BABAR*, Collaboration), Phys. Rev. D **73**, 092001 (2006).
[40] L. Hofer and J. Matias, J. High Energy Phys. 09 (2015) 104.